Influence of self-substitution on the thermoelectric Fe2VAl Heusler alloy

A. Diack-Rasselio, O. Rouleau, L. Coulomb, L. Georgeton, M. Beaudhuin, Jean-Claude Crivello, E. Alleno

Influence of self-substitution on the thermoelectric Fe_2VAl Heusler alloy

A. Diack-Rasselio[1], O. Rouleau[1], L. Coulomb[2], L. Georgeton[2], M. Beaudhuin[2], J.-C. Crivello[1], E. Alleno[1]*

1. Univ. Paris-Est Creteil, ICMPE-CNRS, UMR 7182, 2 rue H. Dunant, F94320 Thiais, FRANCE

2. ICGM, Univ Montpellier, CNRS, ENSCM, Montpellier, France

The microstructure and the thermoelectric properties were systematically determined in the $Fe_2V_{1+x}Al_{1-x}$, $Fe_{2+x}VAl_{1-x}$, $Fe_{2-x}V_{1+x}Al$ series to investigate the influence of self-substitution on the Fe_2VAl Heusler alloy. In the explored range of compositions ($-0.1 < x < 0.1$), all these series are solid solutions, which form anti-site defects to accommodate the off stoichiometry. They all crystallize in the cubic $L2_1$ structure, but their lattice parameter unusually increases with $|x|$. A Bader analysis based on Density Functional Theory calculations indicates that these uncommon lattice parameter changes arise from variations in the interatomic electron transfer. The antisite defects behave like dopants that control the conduction type and charge carrier concentration. This leads to large thermoelectric power factor (PF) in the $Fe_2V_{1+x}Al_{1-x}$ series, which displays the largest electronic mobility. PF = 6.7 mW m^{-1} K^{-2} at 250 K and PF = 3.2 mW m^{-1} K^{-2} at 325 K are reached in *n*-type $Fe_2V_{1.03}Al_{0.97}$ and *p*-type $Fe_2V_{0.985}Al_{1.015}$ respectively. The lattice thermal conductivity systematically decreases upon self-substitution, but with differences among the series which can be traced back to the interatomic electron transfer unveiled by the Bader analysis. Finally, the figure of merit is improved to ZT = 0.06 at 500 K in *p*-type $Fe_2V_{0.93}Al_{1.07}$ and ZT = 0.15 at 420 K in *n*-type $Fe_2V_{1.08}Al_{0.92}$.

* Corresponding author. eric.alleno@cnrs.fr

1.- Introduction

The increasing need of energy to power devices, factories, homes, and the dwindling of natural resources lead to the search of alternative sources, both reliable and renewable. Among those research paths, the conversion of heat to electricity is interesting. Indeed, heat is ubiquitous in manufacturing plants, cars and is primarily wasted in daily activities. One way to convert this wasted heat to electricity is the use of thermoelectric devices. Thermoelectric devices are used primarily for cooling applications (Peltier effect) [1] and power generation (Seebeck effect) [1, 2] but due to their low efficiency, current applications are limited to niche applications, such as powering deep-space missions [3]. However, their indisputable reliability (free of moving parts) and their compacity compensate their performances. They are envisaged for powering autonomous sensors and actuators [4]. To compare and evaluate thermoelectric materials, one uses the dimensionless figure of merit *ZT* defined by the relation:

$$ZT = \frac{\alpha^2 T}{\rho\,(\lambda_e + \lambda_L)}$$

with α the Seebeck coefficient, T the temperature, ρ the electrical resistivity, λ_e and λ_L the electronic and lattice contributions to the total thermal conductivity ($\lambda = \lambda_e + \lambda_L$). The state-of-the-art thermoelectric material at 300 K is Bi_2Te_3 with $ZT = 1$. However, the cost and the toxicity of its constituents prevent its widespread. Fe_2VAl is conversely constituted of earth-abundant chemical elements and when properly doped [5], displays a power factor $PF = \frac{\alpha^2}{\rho}$ > 5 mW m^{-1} K^{-2}, a value larger than that of Bi_2Te_3. Nonetheless, the thermal conductivity is λ = 29 W m^{-1} K^{-1} in pristine Fe_2VAl [5], one order of magnitude larger than in Bi_2Te_3. Substituting V atom by a heavy element such as Ta introduces mass fluctuations in the crystal, which scatter the heat carrying phonons, decreases the thermal conductivity to λ = 10 W m^{-1} K^{-1} and leads to ZT = 0.2 at 400 K [6]. This ZT value is still too low for Fe_2VAl to be considered in applications. Nanostructuring can provide the additional decrease of thermal conductivity

required to improve performances in Fe_2VAl [7]. To fully benefit from this effect and avoid spurious decrease of the power factor upon nanostructuring, a prior and detailed knowledge of the dependence of *PF* on dopant(s) and on charge carrier(s) concentration is a prerequisite. Several references in the literature have experimentally [8] [9] [10] [11] and theoretically [12] [13] [14] shown the occurrence of V_{Al} (V instead of Al) and Al_V (Al instead of V) as "native" antisites defects in stoichiometric Fe_2VAl as well as the occurrence of Fe_V, V_{Fe}, Fe_{Al}, Al_{Fe} antisites defects in off-stoichiometric Fe_2VAl. When compared to antisite defects, the vacancies and interstitials defects indeed display too high enthalpies of formation to exist in these alloys [13]. Depending on their nature, the antisite defects are either electron donors or acceptors and hence strongly influence the electronic transport properties and power factor. Moreover Miyazaki et al. [15] reported a large maximum power factor PF_{max} = 6.8 mW m^{-1} K^{-2} at 300 K in *n*-type $Fe_2V_{1+x}Al_{1-x}$. We thus decided to re-examine the previous series, both *n*- and *p*-type doped and to extend this work to the unknown or nearly unknown $Fe_{2-x}V_{1+x}Al$ and $Fe_{2+x}VAl_{1-x}$ ($-0.1 \leq x \leq 0.1$) series, by comprehensively investigating their microstructural and thermoelectric properties. A theoretical Bader analysis completes this experimental study and provides deep insights on the influence of interatomic electron transfer on the crystal structure and transport properties.

2.- Experimental and theoretical methods

2.1 Synthesis

$Fe_2V_{1+x}Al_{1-x}$, $Fe_{2-x}V_{1+x}Al$ and $Fe_{2+x}VAl_{1-x}$ samples ($-0.1 < x < 0.1$) were prepared by melting adequate quantities of high purity elemental iron (99.97%), vanadium (99.99%) and aluminum (99.98%) in an arc- furnace. To ensure homogeneity, the samples were remelted and flipped over at least four times. Weight losses after melting were less than 0.3%. These samples were subsequently annealed for 72 h at 1173 K in a vacuum-sealed quartz tube and furnace

cooled. Disk-shaped samples with 10 mm diameter and ~ 1 mm thickness were cut with a c-BN wheel saw for electrical resistivity and thermal diffusivity measurements. Ten-millimeter-long bar-shaped samples were subsequently cut for Seebeck coefficient measurements, the remaining part was kept for 3ω thermal conductivity measurement. To remove the microstrains that occur upon cutting, polishing, or grinding [16], each sample was subsequently annealed under secondary vacuum at 1173 K for 2 h, followed by furnace cooling. For X-ray powder diffraction (XRD), the ground powders were similarly annealed before the measurements.

2.2 Microstructural characterization

The samples were structurally characterized by performing powder X-ray diffraction (XRD) on a Bruker D8 diffractometer (Cu-Kα radiation). The lattice parameter of the cubic unit-cell, the line width parameters, the isotropic atomic displacement parameters of these Heusler alloys were refined by the Rietveld method, with the help of the Fullprof program [17]. Microstructural and chemical analyses were carried out by scanning electron microscopy (SEM, Zeiss Merlin) and electron probe micro-analyses (EPMA, Cameca SX100) respectively. The atomic compositions were converted to formula unit by normalizing the total number of atoms to 4. This assumes that no vacancy is considered in these compounds, in agreement with their very large enthalpies of formation (several eV/vacancy) derived from first-principle calculations [13].

2.3 Transport measurements

The Seebeck coefficient and the electrical resistivity were both measured in an argon atmosphere from 150 K to 300 K and from 300 K to 600 K using two home-made apparatus, described in detail in ref. [18] [19]. Thermal diffusivity (a) was measured by the laser flash method using a Netzsch LFA 457 equipment from 300 K to 600 K in an argon atmosphere. The thermal conductivity (λ) was derived using the relationship $\lambda = a \times C_p \times d$ with C_p the heat capacity obtained using the Dulong and Petit's law and d the density measured by Archimedes'

method. From 150 K to 300 K, the thermal conductivity was measured by the 3ω method [20, 21] using a cold finger cryostat and an acquisition setup as described in ref. [22]. The uncertainty values on the Seebeck coefficient, the electrical resistivity, and the thermal conductivity are respectively 6%, 8% and 11% [23]. In some cases, a discrepancy between the laser-flash and the 3ω data smaller than the uncertainty was observed. The latter data were corrected by nullifying the difference at 300 K, with the former data considered as more reliable. The lattice part of the thermal conductivity λ_L was obtained by subtracting the electronic part λ_e, related to the electrical resistivity by the Wiedemann-franz law $\lambda_e = LT/\rho$, with the Lorentz number $L = 2.45 \times 10^{-8}\ V^2\ K^{-2}$.

2.4 Calculations details

To model the substitutional chemical disorder in $Fe_2V_{1+x}Al_{1-x}$, large supercell units have been designed based on $N = 160$ atoms, including $n_{Fe} = 80$, $n_V = 40 + n$ and $n_{Al} = 40 - n$, with $n \in \{0, \pm1, \pm2, \pm3\}$ to describe the 5 compositions from $Fe_2V_{0.925}Al_{1.075}$ to $Fe_2V_{1.075}Al_{0.925}$ with a step of $x = 0.025$. A special attention was required in the choice of atoms distribution for $n = 2$ and 3 where several cases were tested and the most stable one (displaying the lowest energy) was considered.

After the supercell generation, a post-calculation was made to estimate volume, heat of formation and electronic charge transfer in the frame of the Density Functional Theory (DFT) [24]. The DFT calculations were done using pseudopotential and projector augmented wave (PAW) methods [25] as implemented in the VASP code [26] [27]. The Perdew–Burke–Ernzerhof (PBE) functional [28] was considered for the exchange-correlation contribution, whereas spin-orbit coupling was left aside. A plane wave basis set with 600 eV as cutoff energy was used in all calculations converging within 0.1 meV in the total energy under a high-density k-meshing ($\Delta k_u \leq 0.05\ 2\pi/u$, with $u = a$, b or c). For all the compounds, relaxations were

performed so that the convergence of Hellmann-Feynman forces was better than 1 meV $Å^{-1}$ by carefully using separated volume and ionic relaxations in a repetitive steps procedure.

The electronic charge distribution on the atoms was investigated using Bader's topological analysis [29]. In this approach developed initially for molecules, atomic charges are calculated using the decomposition of electronic charge density into atomic contributions by dividing the space into atomic regions with surfaces at a minimum in the charge density. We have used the "Bader" code developed by Henkelman et al. [30].

3.- Results and discussions

3.1 Microstructure

Fig. 1a-c display back-scattered electron (BSE) images of one sample in each alloy series. The variation of contrast observed across each image is related to differing grain orientations. The mean grain size, determined by averaging Feret's diameters [31], is 500 ± 100 μm in $Fe_2V_{0.95}Al_{1.05}$ and $Fe_{1.96}V_{1.04}Al$ (Fig. 1a-b), and 250 ± 50 μm in $Fe_{1.92}VAl_{1.08}$. (Fig. 1c). The smaller grain size in this last sample is most likely related to the position of the polished chunk taken from the melted button, relative to the sole of the arc furnace: the grains are smaller in the button part closer to the water-cooled sole due to a faster cooling rate in this area. Anyway, these grain sizes are large enough to avoid effects on the transport properties. The dark spots can be ascribed to pores and from these images, no secondary phases could be detected. Fig. 1d shows the atomic concentrations measured on 86 randomly selected points on the $Fe_{1.92}VAl_{1.08}$ sample (nominal composition). The average measured composition is $Fe_{1.90(1)}V_{1.03(3)}Al_{1.07(2)}$ with a standard deviation from point to point of 0.01 - 0.03 mol / f.u.. The complete list of samples, their nominal and EPMA compositions are compiled in Table I. Each sample displays a microprobe composition equal, within uncertainty, to its nominal composition.

Fig. 2 presents the XRD patterns of all the samples in the $Fe_2V_{1+x}Al_{1-x}$, $Fe_{2+x}VAl_{1-x}$, $Fe_{2-x}V_{1+x}Al$ series. Every line could be indexed within the $L2_1$ structure type (space group Fm-3m) and no extra line that could have arisen from a secondary phase could be detected. The 111 and 200 lines are well defined on every pattern and characteristic of the $L2_1$ order [16]. In Fig. S1 (Supplementary Material), a typical example of Rietveld refinement in nominal Fe_2VAl shows the good quality of the fit (R_{wp} = 1.9% and R_B = 14.1%) and confirms that these compositions crystallize in the $L2_1$ structure.

The evolution of the refined lattice parameter as a function of composition ($-0.1 < x < 0.1$) for all three series is displayed in Fig. 3. In $Fe_2V_{1+x}Al_{1-x}$ (Fig. 3a), the lattice parameter increases linearly with the absolute value of x, and two Vegard's laws are thus observed, one for each sign of x, with a minimum value $a_{min} = 5.7622 \pm 6 \times 10^{-4}$ Å at $x = -0.01$. This shift from $x = 0.00$ does not indicate that $Fe_2V_{1.01}Al_{0.99}$ rather than Fe_2VAl displays the minimum lattice parameter in the series. It probably rather arises from a systematic deficit of aluminum in these samples due to partial oxidation, which remained undetected by EPMA because it is of the order of its uncertainty (~ 0.01). The linear evolutions of the lattice parameter indicate that $Fe_2V_{1+x}Al_{1-x}$ with $-0.1 < x < 0.1$ is a solid solution where the deviation from stoichiometry is accommodated by the formation of Al_V or V_{Al} antisites defects. This is in good agreement with the literature on this series [15] and moreover $a(x)$ can be linearly extrapolated to the binary alloys FeAl (x = -1) [32] and quenched FeV (x = +1) [33], both crystallizing in the disordered $B2$ structure. Nonetheless, this non-monotonous variation with x cannot be straightforwardly explained by simple arguments: for instance, the difference of atomic radii between V (135 pm) and Al (125 pm) [34] or the valence electron count both evolve monotonously with x. Although the volume increase for $x > 0$ could be easily understood by the geometric criterion, the increase for the Al-richer composition, $x < 0$, is not. To better understand this counter intuitive behavior, we carried out first principles calculations and a Bader analysis, as described in the 2.4

methodology section [30]. This approach partitions the space into volumes to weigh the contribution of each atom to the bonding. Each Bader volume contains a single charge density maximum and is separated from other volumes by surfaces on which the charge density is a minimum normal to these surfaces [35, 36]. The Bader volumes and charges arising from the present analysis are centered on the atomic nuclei. Figure 4.a compares the cell parameter from theoretical results with the experiments in $Fe_2V_{1+x}Al_{1-x}$. The absolute theoretical and experimental values do not agree due to the underestimation of the actual unit-cell volume using GGA-PBE approximation. However, the relative experimental variation rate of *a(x)* for $x < 0$ is nearly quantitatively represented by the theory, whereas *a(x)* for $x > 0$ is not described quantitatively but qualitatively, the experimental slope being underestimated for $x > 0$. Theory also confirms that the $x = 0$ composition displays the minimum lattice parameter, in agreement with the experiment. These increases of *a* with $|x|$ can be related to the variations of the atomic Bader volumes (Fig. 4 b). For $x < 0$, it can be noticed that both the Fe and Al volumes increase with $|x|$, while for $x > 0$, only the Al volume increases. These variations of the Bader atomic volumes can be related to the variations with *x* of the Bader charge displayed in Fig. 4b. Before commenting the variations with *x*, it is necessary to interpret the value and sign of the Bader charge (q) for each atom at $x = 0$. Both Al and V display a positive charge (+1.8 and +0.8 respectively) while Fe displays a negative charge (-1.3). Since $2q_{Fe} + q_V + q_{Al} = 0$ for any *x*, this means that a "net transfer" of part of the Al and V electron towards Fe occurs. This net transfer is only partial because $q_{Al} \neq +3$, $q_V \neq +5$ and $q_{Fe} \neq -4$, the valence of Al and V and the number of empty 3*d* states in Fe, respectively. Fe_2VAl can thus be understood as a partially ionic or "charge transfer" compound with the effective formula $Fe_2^{1.3-}V^{0.8+}Al^{1.8+}$, where V and Al behave like cations and Fe like an anion. This electron transfer is explained by the progressive 3*d*-Fe bands filling from the electrons of cations, leading to a more stable electronic structure for the compound. This scheme disagrees with the scheme $Fe_2^{1-}V^{1-}Al^{3+}$

proposed in ref. [37], which was based on simpler electronegativity considerations. It agrees with the Bader analysis [38] performed in the half-Heusler $Li^{1+}Al^{1+}Si^{2-}$ or $Li^{1+}Al^{1+}Ge^{2-}$ compounds, where both most electropositive atoms transfer part of their electrons to the most electronegative one. More importantly, it agrees well with the interatomic charge transfers reported in ref. [39] for Fe_2VAl, where $Fe_2^{0.75-}V^{0.5+}Al^{1.0+}$ was derived from a similar Bader analysis. For $x < 0$ and upon increasing $|x|$, the Bader charge of Fe and Al decreases or becomes more negative, while the charge of V increases or becomes more positive, indicating a stronger electron transfer from the latter atom towards the two former atoms. This leads to the expansion of the Bader volume of Fe and Al due to their larger electron population. For increasing $x > 0$, as already mentioned, these calculations only capture the decrease of the Al charge and misses the decrease of the charge of either the Fe or V atom. We can nonetheless surmise that the electron transfer from the Al atom to either Fe, V or both atoms, leads to their volume expansion and to the increase of *a(x)*. To summarize, these variations of the lattice parameter in $Fe_2V_{1+x}Al_{1-x}$ can be explained by varying electron transfers with *x*, between the constituting atoms.

Figures 3c and 3b display the lattice parameters for the alloy series $Fe_{2-x}V_{1+x}Al$ and $Fe_{2+x}VAl_{1-x}$ respectively. In the case of $Fe_{2-x}V_{1+x}Al$, a Vegard's law is obvious for $x \geq 0$. It becomes apparent for $x \leq 0$ when considering values of $|x|$ up to 0.4 (see inset of Fig. 3c). Nishino et al. presented a similar report on the evolution of the lattice parameter in $Fe_{2-x}V_{1+x}Al$ for $-1 \leq x \leq 0.2$ [40]. For $Fe_{2+x}VAl_{1-x}$, two Vegard's laws are also observed for $x \geq 0$ and $x \leq 0$. These two series hence follow a solid solution behavior, at least for $-0.1 < x < 0.1$. Again, the deviation from stoichiometry is accommodated in these series by the formation of antisite defects such as Al_{Fe}, Fe_{Al}, Fe_V or V_{Fe}. Similarly, to the first series, a minimum value is also observed close to $x = 0$ in $Fe_{2-x}V_{1+x}Al$ and $Fe_{2+x}VAl_{1-x}$. Nonetheless, it is difficult to determine accurately its *x*-position due an insufficient number of data points in this neighborhood.

Currently, the best estimation is a_{min} = 5.7633 ± 6 × 10^{-4} Å at x = 0 for both series, in good agreement with the minimum value derived from the $Fe_2V_{1+x}Al_{1-x}$ series. Nonetheless, a systematic elemental deficit cannot currently be detected from the $a(x)$ data in $Fe_{2+x}VAl_{1-x}$. Following the Bader analysis of $Fe_2V_{1+x}Al_{1-x}$, the evolutions of the lattice parameters in $Fe_{2+x}VAl_{1-x}$ and $Fe_{2-x}V_{1+x}Al$ for each sign of x can most probably be ascribed to variations in the charge transfers between the constituting atoms. As will be further discussed, the antisite defects formed in these three series can modify the electronic transport properties of these alloys.

3.2 Electronic transport properties

3.2.1 Electrical properties at room temperature

The values of carrier concentrations, carrier mobilities, Seebeck coefficient, resistivity and power factor measured at 300 K in $Fe_2V_{1+x}Al_{1-x}$, $Fe_{2+x}VAl_{1-x}$ and $Fe_{2-x}V_{1+x}Al$ are presented in Table I and II, respectively. In agreement with the literature [41] [10] [42], pristine Fe_2VAl displays a *p*-type conduction with a concentration of 3.9 × 10^{20} holes cm^{-3} as majority charge carriers. Upon self-substitution in $Fe_2V_{1+x}Al_{1-x}$, as expected [15], the formation of Al_V defects in Al-rich compositions (x < 0) leads to *p*-type conduction whereas the formation of V_{Al} counterpart defects in V-rich compositions (x > 0) leads to *n*-type conduction. We previously discussed that in pristine Fe_2VAl, the formation of few percent of combined Al_V - V_{Al} antisite defects ("inversions") leads to the observed hole concentration at 300 K [43]. Similarly, Fe_V, Al_{Fe} antisite defects and V_{Fe}, Fe_{Al} as their counterparts are presently shown to give rise to *p*- and *n*-type conduction in $Fe_{2-x}V_{1+x}Al$ and $Fe_{2+x}VAl_{1-x}$, respectively. The antisite defects formed in these three series hence behave either as electron acceptors or electron donors and control the electronic transport properties. As previously discussed in the Bader analysis, a stronger electron transfer from the V atom towards the Al atom occurs in $Fe_2V_{1+x}Al_{1-x}$ for x < 0 and it thus accompanies the electron acceptor character of the Al_V defects. Similarly, a stronger

electron transfer towards the V atom occurs for $x > 0$, when V_{Al} defects behave as electron donor. This is in line with atom-projected density of states (*p*-DOS) calculations in Fe_2VAl [16] [37] that shows that V and Fe e_g states contribute strongly to the conduction band.

In Table II, when comparing the $Fe_2V_{1+x}Al_{1-x}$, $Fe_{2-x}V_{1+x}Al$ and $Fe_{2+x}VAl_{1-x}$ series, the Seebeck coefficient reaches the remarkable values of +93.2 μV K^{-1} in *p*-type samples and -151.6 μV K^{-1} in *n*-type samples. For both types, α and ρ vary according to *x* and *p* or *n*: except Fe_2VAl, the samples with the compositions the closest to the stoichiometry display the largest absolute value of the Seebeck coefficient and resistivity and the smallest charge carrier concentration, whereas the most off-stoichiometric samples display the smallest values of α and ρ and the largest values of *p* or *n*.

It can also be noticed in Table I that for every series, the electronic mobility is three- to four-time larger in *p*-type compositions than in their *n*-type counterpart. For instance, it is in the range 25 – 40 cm^2 V^{-1} s^{-1} for *p*-type $Fe_2V_{1+x}Al_{1-x}$ while it is in the range 7 – 12 cm^2 V^{-1} s^{-1} for *n*-type $Fe_2V_{1+x}Al_{1-x}$. When comparing compositions with similar electron and hole concentration, a ratio $\frac{\mu_p}{\mu_n} = 3.6$ can be derived. Since this feature is also effective at least in the other $Fe_{2+x}VAl_{1-x}$ series, it is independent on the nature of the dopant and is very likely to arise from the band structure of Fe_2VAl *e.g.*, a smaller effective mass for the holes than the electrons. When comparing the 3 series between each other, for a given type of conduction, the electronic mobility is many-fold larger in $Fe_2V_{1+x}Al_{1-x}$ than in $Fe_{2-x}V_{1+x}Al$ and $Fe_{2+x}VAl_{1-x}$. The reduced mobility in the last two series is related to the occurrence of Fe_V, Al_{Fe}, V_{Fe}, Fe_{Al} defects, which either modify the electronic structure or scatter more strongly the charge carriers than the Al_V or V_{Al} defects. Based on DFT calculations [12, 13], Fe_V Fe_{Al} and V_{Fe} have been reported to be magnetic defects, whereas V_{Al} has been reported to be non-magnetic. The magnetic character of the former defects may enhance their scattering cross-section of the charge carriers, leading

to a reduced mobility. The V_{Fe} and Fe_{Al} defects have also been predicted [12] to modify the electronic structure by inducing new in-gap states close to the conduction and valence bands. These states could act as charge carrier scatterers of the holes or electrons transported in the main valence and conduction bands states. Magnetic defects and / or new in-gap states are the two scenarios that could explain the reduced electronic mobility in $Fe_{2-x}V_{1+x}Al$ and $Fe_{2+x}VAl_{1-x}$.

It is easily noticeable that the larger observed values of mobility in the $Fe_2V_{1+x}Al_{1-x}$ series than in the $Fe_{2-x}V_{1+x}Al$ and $Fe_{2+x}VAl_{1-x}$ series (Table I) lead systematically to smaller values of resistivity in the former series than in the latter (Table II). Remarkably, in $Fe_2V_{1+x}Al_{1-x}$, ρ is always smaller than 2.5 μΩ m and 5 μΩ m in *p*- and *n*-type compounds respectively. This leads to large values of PF in (Table II) in $Fe_2V_{1+x}Al_{1-x}$. For $Fe_{2-x}V_{1+x}Al$ and $Fe_{2+x}VAl_{1-x}$, irrespective of their conduction type, values of *PF* do not exceed 1.6 mW m^{-1} K^{-2} whereas a value as large as *PF* = 5.8 mW m^{-1} K^{-2} is observed in *n*-type $Fe_2V_{1+x}Al_{1-x}$. Measurements as a function of temperature will confirm that the latter series presents better thermoelectric properties than the others. When comparing *n*-type with *p*-type $Fe_2V_{1+x}Al_{1-x}$, the previously unveiled correlation between μ and *PF* does not apply anymore: despite larger mobility values in *p*-type $Fe_2V_{1+x}Al_{1-x}$, only a smaller value of *PF* = 3.2 mW m^{-1} K^{-2} is obtained in *p*-type $Fe_2V_{0.985}Al_{1.015}$. Since the power factor is not optimized for any conduction type, it is difficult to draw a definitive conclusion on this difference, but it is likely to be related to electrons displaying a larger effective mass than holes.

3.2.2 Evolution of the electrical properties with temperature

The Seebeck coefficient, resistivity and power factor measured between 100 K and 600 K are displayed as a function of temperature in Fig. 5, 6, 7 and 8 for $Fe_2V_{1+x}Al_{1-x}$, $Fe_{2-x}V_{1+x}Al$ and $Fe_{2+x}VAl_{1-x}$ respectively. In the $Fe_2V_{1+x}Al_{1-x}$ series, the electrical resistivity (Fig. 5b, 6b) goes through a maximum in the temperature range 300 K – 600 K in both *p*-type or *n*-type

compounds. This behavior is characteristic of degenerate semi-conductors: at temperatures smaller than the maximum their metal-like electrical transport is dominated by the electrons (holes) with their chemical potential in the conduction (valence) band(s) and at temperature larger than the maximum, their semiconducting-like behavior is dominated by the minority carriers excited across the gap. Similarly, the Seebeck coefficient (Fig. 5a, 6a) displays a maximum or a minimum in *p*-type or *n*-type $Fe_2V_{1+x}Al_{1-x}$ compositions respectively. These extrema fall in the range [270 K – 520 K] and are shifted by roughly -100 K when compared to the corresponding electrical resistivity maximum. This point has been discussed in $Co_{1-x}Ni_xSb_3$ by Kajikawa [44] who ascribed it to the occurrence of several bands for the minority carriers, all contributing to the electrical conductivity and the Seebeck coefficient, but at different temperatures due to differing mobilities in the bands. Again, these variations are typical of degenerate semiconductors entering the intrinsic regime at high temperature. Consequently, depending on composition, the power factor (Fig. 5c, 6c) shows a maximum between 250 K and 500 K. It reaches PF_{max} = 6.7 mW m^{-1} K^{-2} and PF_{max} = 3.2 mW m^{-1} K^{-2} in *n*-type $Fe_2V_{1.03}Al_{0.97}$ at 250 K and in *p*-type $Fe_2V_{0.985}Al_{1.015}$ at 325 K respectively. The present *n*-type maximum power factor is as large as the one reported in ref. [15] for $Fe_2V_{1+x}Al_{1-x}$, whereas the maximum *p*-type power factor is slightly smaller. This confirms anyway that PF_{max} is larger in Fe_2VAl than in Bi_2Te_3.

In the $Fe_{2-x}V_{1+x}Al$ series, the electrical resistivity (Fig. 7b) shows an activated behavior for both types of conduction in the entire measured temperature range. When compared to the $Fe_2V_{1+x}Al_{1-x}$ series which is degenerate for the present *x* values, the activated behavior most likely arises from a deeper donor (acceptor) level(s) in the *n*-type (*p*-type) compounds of the $Fe_{2-x}V_{1+x}Al$ series. This scenario is supported by electron concentration versus temperature data derived from Hall effect and presented in Fig. S2. The electron concentration shows an activated behavior in $Fe_{1.92}V_{1.08}Al$ whereas it is weakly temperature dependent in $Fe_2V_{1.03}Al_{0.97}$ as

expected in a degenerate semi-conductor. The larger values of electrical resistivity for the *n*-type compositions than the *p*-type ones could be ascribed to a donor level deeper than the acceptor level. At temperatures larger than 400 K, the electrical resistivity values for all the samples converge on a common curve, a feature characteristic of a common regime *e.g.*, the intrinsic regime. The variations of the Seebeck coefficient with temperature (Fig. 7a) are also consistent for both types of conduction with this picture of extrinsic semi-conductors at "low" temperature, entering the intrinsic regime at "high" temperature. The Seebeck coefficient indeed displays a maximum or a minimum in the range [250 K– 350 K] in *p*-type or *n*-type $Fe_{2-x}V_{1+x}Al$ compositions respectively. Again, at temperature smaller than the extremum, transport is dominated by the majority carriers whereas at temperatures larger than the extremum, the minority carriers excited across the gap dominate transport. The power factor varies with temperature in accordance with the Seebeck coefficient: it displays a maximum between 250 K and 350 K. The best maximum power factor value is observed in *p*-type $Fe_{2.04}V_{0.96}Al$ where it reaches PF_{max} = 1.7 mW m^{-1} K^{-2}. The better *p*-type than *n*-type power factor can this time be related to the larger electronic mobility for the former type of conduction than for the latter.

Finally, in the $Fe_{2+x}VAl_{1-x}$ series, the electronic transport (Fig. 8) shows great similarity with the $Fe_{2-x}V_{1+x}Al$ series. The electrical resistivity (Fig. 8.b) is also activated in both *n*- and *p*-type samples in the entire temperature range 120 K – 600 K, it converges towards common values above 400 K and the Seebeck coefficient (Fig. 8.a) exhibits an extremum between 250 K and 300 K. Again, these variations of the electrical resistivity and the Seebeck coefficient are characteristic of extrinsic semi-conductors at temperature below 250 K – 300 K, entering the intrinsic regime at higher temperatures. The best power factor value is obtained in *n*-type $Fe_{2.08}VAl_{0.92}$ at 300 K where PF_{max} = 1.56 mW m^{-1} K^{-2} is reached. This value is significantly

smaller than those reached in *n*-type $Fe_2V_{1+x}Al_{1-x}$. due to an overall larger electronic mobility in the latter series.

3.3 Thermal conductivity and *ZT*

The lattice thermal conductivity (λ_L) for all three series is plotted in Fig. 9. In each sample, this quantity decreases monotonously with temperature, due to the increasing phonon – phonon interaction. Among all the sample, Fe_2VAl displays the largest values with λ_L = 26 W m^{-1} K^{-1} at 300 K, in agreement with previous studies [5]. The off-stoichiometric compositions systematically display smaller values than in Fe_2VAl, and for a given sign of *x*, in all three series, λ_L decreases with increasing $|x|$. This arises from the scattering of phonons by the masses and interatomic force constants (IFCs) fluctuations introduced by the self-substitutions. Theory [45] allows to formulate explicitly both contributions: the perturbation term to the dynamic Hamiltonian can be written as $V = -\frac{\Delta m_i}{m_i}\omega^2 + \frac{\Delta k_{ij}}{\sqrt{m_i m_j}}$ where m_i and k_{ij} refers to the unperturbed mass of atom in site *i* and the IFCs between site *i* and *j* respectively. Δm_i and Δk_{ij} refer to the difference between the perturbed and the unperturbed mass and IFCs respectively. On the one hand, in the $Fe_2V_{1+x}Al_{1-x}$ series, λ_L varies from sample to sample in accordance with their departure from stoichiometry ($|x|$), regardless of the sign of *x*: the $x = \pm 0.03$ and the $x = \pm 0.07$ display very close values of λ_L on broad ranges of temperature. This means that the inequivalent modifications of the IFCs arising from excess Al or excess V weakly affect the lattice thermal conductivity and the mass term, which is symmetric with both Al or V excesses, dominates the perturbation Hamiltonian for this series. In a recent article [43], it has also been shown theoretically and experimentally that in $Fe_2V_{1-x}Ta_xAl_{1-x}Sn_x$ where similarly to $Fe_2V_{1+x}Al_{1-x}$ only the V and Al sites are substituted, the mass term dominates over the IFCs contribution to the perturbation. On the other hand, in the $Fe_{2-x}V_{1+x}Al$ and $Fe_{2+x}VAl_{1-x}$ series, λ_L depends on the sign of *x* and is smaller when Fe is in excess, rather than V or Al. This implies

that the IFCs or "chemical bonding strength" are more perturbed when Fe substitutes V or Al than the opposite situations. It can be surmised that this specific effect of Fe on λ_L could be related to the effective formula $Fe_2^{1.3-}V^{0.8+}Al^{1.8+}$ derived from the present Bader analysis. Indeed, Fe behaves in Fe_2VAl like an anion, whereas V and Al behave like cations. Exchanging V and Al *e.g.* two cations most likely affects less strongly the chemical bonds or IFCs than exchanging an anion with a cation. Despite these differing behaviors with x among the three series, the smallest values of λ_L reached for $x = \pm 0.08$ in every series are very close to 13 W m^{-1} K^{-1} at 300 K, regardless of the series. This value is too large to ensure large figures of merit in these compositions, as will be discussed in the next part.

The dimensionless figure of merit (ZT) is plotted as a function of temperature in Fig. 10 for $Fe_2V_{1+x}Al_{1-x}$ and in Fig. 11 for $Fe_{2-x}V_{1+x}Al$ and $Fe_{2+x}VAl_{1-x}$. For every composition, ZT mimics the variations with temperature of the power factor: it increases with temperature at low temperature, passes through a maximum and decreases at high temperature. As previously discussed, this maximum and this decrease arise from the adverse contribution of minority carriers at high temperature. In p-type $Fe_2V_{1+x}Al_{1-x}$, the largest figure of merit $ZT_{max} = 0.06$ is reached at 500 K in $Fe_2V_{0.93}Al_{1.07}$ whereas n-type $Fe_2V_{1.08}Al_{0.92}$ remarkably displays $ZT_{max} = 0.15$ at 450 K. Miyazaki et al. [15] previously reported $ZT_{max} = 0.04$ in p-type $Fe_2V_{0.97}Al_{1.03}$ and $ZT_{max} = 0.13$ in n-type $Fe_2V_{1.07}Al_{93}$, values slightly smaller than the present ones. In the $Fe_{2-x}V_{1+x}Al$ and $Fe_{2+x}VAl_{1-x}$ series, the figure of merit is systematically smaller than in $Fe_2V_{1+x}Al_{1-x}$., similarly to the power factor. It nonetheless reaches at 400 K $ZT_{max} = 0.03$ in p-type $Fe_{2.04}V_{0.96}Al$ and $ZT_{max} = 0.04$ in n-type $Fe_{2.08}VAl_{0.92}$.

Despite large values of power factor (~ 3 – 6 mW m^{-1} K^{-2}) leading to figure of merit larger or at the state of the art, the overall too large thermal conductivity – minimum λ ~ 15 W m^{-1} K^{-1} at 300 K – found in these three series hampers their performances. As already discussed in the introduction, further decrease of the thermal conductivity either by substituting

other elements or by nanostructuring are required to reach *ZT* values high enough to envisage thermoelectric applications for Fe_2VAl.

4. Summary

All these $Fe_2V_{1+x}Al_{1-x}$, $Fe_{2-x}V_{1+x}Al$ and $Fe_{2+x}VAl_{1-x}$ alloys crystallize in the $L2_1$ Heusler structure and all display a solid solution behavior in the explored composition range ($-0.1 < x < 0.1$). The off stoichiometry is accommodated by the formation of anti-site defects such as Al_V, V_{Al}, Fe_V, V_{Fe}, Fe_{Al} and Al_{Fe}. Based on DFT calculations, the electronic Bader analysis indicates that Fe_2VAl can be seen as a "charge transfer" compound with the effective formula $Fe_2^{1.3-}V^{0.8+}Al^{1.8+}$ and that the unit-cell volume change occurring with *x* in the $Fe_2V_{1+x}Al_{1-x}$ series can be understood by variations of these interatomic charge transfer. The antisite defects are either electron donor or acceptor and control the conduction type and charge carrier concentration. Regardless of the conduction type, the $Fe_2V_{1+x}Al_{1-x}$ series display larger electronic mobility values than the other two series. This leads to larger power factor in the former series than in the two latter: PF_{max} = 6.7 mW m^{-1} K^{-2} at 250 K and PF_{max} = 3.2 mW m^{-1} K^{-2} at 325 K are reached in *n*-type $Fe_2V_{1.03}Al_{0.97}$ and *p*-type $Fe_2V_{0.985}Al_{1.015}$ respectively. The off-stoichiometry leads to a decrease of the lattice thermal conductivity, only due to mass fluctuations in $Fe_2V_{1+x}Al_{1-x}$, whereas it also arises from interatomic force constant fluctuations in $Fe_{2-x}V_{1+x}Al$ and $Fe_{2+x}VAl_{1-x}$ where anionic Fe is substituted to or by cationic V or Al. Finally, figures of merit ZT_{max} = 0.06 at 500 K in *p*-type $Fe_2V_{0.93}Al_{1.07}$ and ZT_{max} = 0.15 at 450 K in *n*-type $Fe_2V_{1.08}Al_{0.92}$ are reached.

Acknowledgments

ICGM would like to thank C. Riebel, A. Viera e Silva, F. Pichot and J.-M. Peyris for their technical support. Funding of this work by the ”Agence Nationale de la Recherche” through the contract ‘‘LoCoThermH’’ (Project ANR-18-CE05-0013-01) is also acknowledged.

References

[1] S. LeBlanc, S.K. Yee, M.L. Scullin, C. Dames, K.E. Goodson, Material and manufacturing cost considerations for thermoelectrics, Renewable and Sustainable Energy Reviews 32(0) (2014) 313-327.

[2] N. Jaziri, A. Boughamoura, J. Müller, B. Mezghani, F. Tounsi, M. Ismail, A comprehensive review of Thermoelectric Generators: Technologies and common applications, Energy Reports 6 (2020) 264-287.

[3] L. Yang, Z.-G. Chen, M.S. Dargusch, J. Zou, High Performance Thermoelectric Materials: Progress and Their Applications, Advanced Energy Materials 8(6) (2018) 1701797.

[4] L.E. Bell, Cooling, Heating, Generating Power, and Recovering Waste Heat with Thermoelectric Systems, Science 321(5895) (2008) 1457.

[5] Y. Nishino, S. Deguchi, U. Mizutani, Thermal and transport properties of the Heusler-type $Fe_2VAl_{1-x}Ge_x$ ($0 < x < 0.20$) alloys: Effect of doping on lattice thermal conductivity, electrical resistivity, and Seebeck coefficient, Physical Review B 74(11) (2006) 115115.

[6] K. Renard, A. Mori, Y. Yamada, S. Tanaka, H. Miyazaki, Y. Nishino, Thermoelectric properties of the Heusler-type Fe2VTaxAl1-x alloys, Journal of Applied Physics 115(3) (2014) 033707.

[7] E. Alleno, Review of the Thermoelectric Properties in Nanostructured Fe2VAl, Metals 8(11) (2018) 864.

[8] A. Matsushita, T. Naka, Y. Takano, T. Takeuchi, T. Shishido, Y. Yamada, Pseudogap and transport properties in Fe3-xVxAly x = 0.5–1.05; y = 0.95,1.05, Physical Review B 65(7) (2002) 075204.

[9] Y. Nishino, H. Sumi, U. Mizutani, Transport and magnetic properties of the Heusler-type Fe2-xV1+xAl system (-0.01<=x<=0.08), Physical Review B 71 (2005) 094425.

[10] C.S. Lue, Y.K. Kuo, Thermoelectric properties of the semimetallic Heusler compounds $Fe_{2-x}V_{1+x}M$ (M=Al, Ga), Physical Review B 66 (2002) 085121.

[11] T. Sugiura, Y. Nishino, Doping Effects of Transition Metals on Thermoelectric Properties of Off-Stoichiometric Fe2VAl Alloys, Journal of the Japan Institute of Metals 73(11) (2009) 846-851.

[12] D.I. Bilc, P. Ghosez, Electronic and thermoelectric properties of Fe_2VAl: The role of defects and disorder, Physical Review B 83(20) (2011) 205204.

[13] S. Bandaru, P. Jund, Electronic structure of the Heusler compound Fe2VAl and its point defects by ab initio calculations, physica status solidi (b) 254(2) (2017) 1600441-n/a.

[14] A. Berche, M.T. Noutack, M.L. Doublet, P. Jund, Unexpected band gap increase in the Fe2VAl Heusler compound, Materials Today Physics 13 (2020) 100203.

[15] H. Miyazaki, S. Tanaka, N. Ide, K. Soda, Y. Nishino, Thermoelectric properties of Heusler-type off-stoichiometric Fe2V1+ xAl1-x alloys, Materials Research Express 1(1) (2014) 015901.

[16] S. Maier, S. Denis, S. Adam, J.-C. Crivello, J.-M. Joubert, E. Alleno, Order-disorder transitions in the Fe2VAl Heusler alloy, Acta Materialia 121 (2016) 126.

[17] J. Rodriguez-Carvajal, FULLPROF, Physica B 192 (1993) 55-69.

[18] D. Bérardan, E. Alleno, C. Godart, O. Rouleau, J. Rodriguez-Carvajal, Preparation and chemical properties of the skutterudites $(Ce\text{-}Yb)_yFe_{4-x}(Co/Ni)_xSb_{12}$, Materials Research Bulletin 40(3) (2005) 537-551.

[19] O. Rouleau, E. Alleno, Measurement system of the Seebeck coefficient or of the electrical resistivity at high temperature, Review of Scientific Instruments 84(10) (2013) 105103.

[20] D.G. Cahill, Thermal-Conductivity Measurement from 30-K to 750-K - the 3-Omega Method, Review of Scientific Instruments 61(2) (1990) 802-808.

[21] M. Beaudhuin, Mesure de la conductivité thermique par la méthode 3-oméga, Techniques de l'ingénieur Mesures physiques base documentaire : TIP672WEB(ref. article : r2918) (2019).

[22] I. Sinnarasa, Y. Thimont, A. Barnabé, M. Beaudhuin, A. Moll, J. Schorne-Pinto, P. Tailhades, L. Presmanes, Microstructural and transport properties of Mg doped CuFeO2 thin films: A promising material for high accuracy miniaturized temperature sensors based on the Seebeck effect, Journal of Alloys and Compounds 827 (2020) 154199.

[23] E. Alleno, D. Bérardan, C. Byl, C. Candolfi, R. Daou, R. Decourt, E. Guilmeau, S. Hébert, J. Hejtmanek, B. Lenoir, P. Masschelein, V. Ohorodnichuk, M. Pollet, S. Populoh, D. Ravot, O. Rouleau, M. Soulier, Invited Article: A round robin test of the uncertainty on the measurement of the thermoelectric dimensionless figure of merit of Co0.97Ni0.03Sb3, Review of Scientific Instruments 86(1) (2015) 011301.

[24] W. Kohn, L.J. Sham, Self-Consistent Equations Including Exchange and Correlation Effects, Physical Review 140(4A) (1965) A1133-A1138.

[25] P.E. Blöchl, Projector augmented-wave method, Physical Review B 50(24) (1994) 17953-17979.

[26] G. Kresse, J. Furthmüller, Efficiency of ab-initio total energy calculations for metals and semiconductors using a plane-wave basis set, Computational Materials Science 6(1) (1996) 15-50.

[27] G. Kresse, D. Joubert, From ultrasoft pseudopotentials to the projector augmented-wave method, Physical Review B 59(3) (1999) 1758-1775.

[28] J.P. Perdew, K. Burke, M. Ernzerhof, Generalized Gradient Approximation Made Simple, Physical Review Letters 77(18) (1996) 3865-3868.

[29] R.F.W. Bader, Atoms in Molecules: A Quantum Theory Oxford University Press, New York, 1990.

[30] G. Henkelman, A. Arnaldsson, H. Jónsson, A fast and robust algorithm for Bader decomposition of charge density, Computational Materials Science 36(3) (2006) 354-360.

[31] H.J. Hofmann, Chapter 2.5 Stromatoid Morphometrics, in: M.R. Walter (Ed.), Developments in Sedimentology, Elsevier1976, pp. 45-54.

[32] D. Mondal, S. Banik, C. Kamal, M. Nand, S.N. Jha, D.M. Phase, A.K. Sinha, A. Chakrabarti, A. Banerjee, T. Ganguli, Electronic structure of FeAl alloy studied by resonant photoemission spectroscopy and Ab initio calculations, Journal of Alloys and Compounds 688 (2016) 187-194.

[33] J.I. Seki, M. Hagiwara, T. Suzuki, Metastable order-disorder transition and sigma phase formation in Fe-V binary alloys, Journal of Materials Science 14(10) (1979) 2404-2410.

[34] https://www.webelements.com/, The periodic table of the elements, accessed March 2022.

[35] W. Tang, E. Sanville, G. Henkelman, A grid-based Bader analysis algorithm without lattice bias, Journal of Physics: Condensed Matter 21(8) (2009) 084204.

[36] C. Lepetit, P. Fau, K. Fajerwerg, M.L. Kahn, B. Silvi, Topological analysis of the metal-metal bond: A tutorial review, Coordination Chemistry Reviews 345 (2017) 150-181.

[37] S. Anand, R. Gurunathan, T. Soldi, L. Borgsmiller, R. Orenstein, G.J. Snyder, Thermoelectric transport of semiconductor full-Heusler VFe2Al, Journal of Materials Chemistry C 8(30) (2020) 10174-10184.

[38] D. Bende, Y. Grin, F.R. Wagner, Covalence and Ionicity in MgAgAs-Type Compounds, Chemistry – A European Journal 20(31) (2014) 9702-9708.

[39] B. Hinterleitner, F. Garmroudi, N. Reumann, T. Mori, E. Bauer, R. Podloucky, The electronic pseudo band gap states and electronic transport of the full-Heusler compound Fe2VAl, Journal of Materials Chemistry C 9(6) (2021) 2073-2085.

[40] Y. Nishino, C. Kumada, S. Asano, Phase stability of Fe3Al with addition of 3d transition elements, Scripta Materialia 36(4) (1997) 461-466.

[41] Y. Nishino, H. Kato, M. Kato, U. Mizutani, Effect of off stoichiometry on the transport properties of the Heusler type Fe2VAl compound, Physical Review B 63 (2001) 233303.

[42] F. Garmroudi, A. Riss, M. Parzer, N. Reumann, H. Müller, E. Bauer, S. Khmelevskyi, R. Podloucky, T. Mori, K. Tobita, Y. Katsura, K. Kimura, Boosting the thermoelectric performance of Fe2VAl Heusler compounds by band engineering, Physical Review B 103(8) (2021) 085202.

[43] M.S.T. Noutack, A. Diack-Rasselio, E. Alleno, P. Jund, Numerical and experimental determination of the thermal conductivity of pristine and substituted Fe2VAl, Journal of Alloys and Compounds 883 (2021) 160828.

[44] Y. Kajikawa, Multi-band analysis of thermoelectric properties of n-type Co1-xNixSb3 ($0<x<0.01$) over a wide temperature range of 10-773 K., Journal of Alloys and Compounds 664 (2016) 338-350.

[45] N.A. Katcho, J. Carrete, W. Li, N. Mingo, Effect of nitrogen and vacancy defects on the thermal conductivity of diamond: An ab initio Green's function approach, Physical Review B 90(9) (2014) 094117.

Table I: Nominal compositions, EPMA compositions, charge carrier concentrations, Hall mobilities in the alloy series $Fe_2V_{1+x}Al_{1-x}$, $Fe_{2+x}VAl_{1-x}$, $Fe_{2-x}V_{1+x}Al$ at 300 K. Negative carrier concentrations correspond to electron as majority carriers.

Nom. Comp.	**EPMA Comp.**	***n* / *p* (10^{20} cm^{-3})**	**μ ($cm^2.V^{-1}.s^{-1}$)**
$Fe_2V_{0.93}Al_{1.07}$	$Fe_{2.00(1)}V_{0.93(1)}Al_{1.07(1)}$	22.4	25.3
$Fe_2V_{0.95}Al_{1.05}$	$Fe_{2.00(1)}V_{0.96(1)}Al_{1.04(1)}$	16.9	30.6
$Fe_2V_{0.97}Al_{1.03}$	$Fe_{1.99(1)}V_{0.98(1)}Al_{1.03(1)}$	11.7	40.2
$Fe_2V_{0.985}Al_{1.015}$	$Fe_{1.99(1)}V_{1.00(1)}Al_{1.01(1)}$	6.97	35.8
Fe_2VAl	$Fe_{2.00(1)}V_{1.01(1)}Al_{0.99(1)}$	3.90	25.8
$Fe_2V_{1.02}Al_{0.98}$	$Fe_{1.97(1)}V_{1.04(2)}Al_{0.99(1)}$	-11.4	11.5
$Fe_2V_{1.03}Al_{0.97}$	$Fe_{2.00(1)}V_{1.04(1)}Al_{0.96(1)}$	-15.3	10.4
$Fe_2V_{1.08}Al_{0.92}$	$Fe_{1.99(1)}V_{1.08(1)}Al_{0.93(1)}$	-37.4	7.7
$Fe_{1.92}V_{1.08}Al$	$Fe_{1.92(1)}V_{1.09(1)}Al_{0.99(1)}$	-41.5	1.0
$Fe_{1.95}V_{1.05}Al$	$Fe_{1.93(2)}V_{1.07(2)}Al_{1.00(1)}$	-39.9	1.1
$Fe_{1.96}V_{1.04}Al$	$Fe_{1.95(1)}V_{1.05(1)}Al_{1.00(1)}$	-34.8	1.5
$Fe_{2.04}V_{0.96}Al$	$Fe_{2.05(1)}V_{0.95(2)}Al_{1.00(2)}$	5.40	22.0
$Fe_{2.08}V_{0.92}Al$	$Fe_{2.08(1)}V_{0.92(1)}Al_{1.00(1)}$	7.35	13.4
$Fe_{1.92}VAl_{1.08}$	$Fe_{1.90(1)}V_{1.03(3)}Al_{1.07(2)}$	11.3	5.6
$Fe_{1.95}VAl_{1.05}$	$Fe_{1.92(3)}V_{1.02(5)}Al_{1.05(5)}$	-	-
$Fe_{2.04}VAl_{0.96}$	$Fe_{2.03(2)}V_{1.01(2)}Al_{0.96(1)}$	12.2	6.3
$Fe_{2.08}VAl_{0.92}$	$Fe_{2.07(1)}V_{1.01(1)}Al_{0.92(1)}$	-34.6	2.4

Table II: Seebeck coefficients, electrical resistivities and power factors (*PF*) in the alloy series $Fe_{2+x}VAl_{1-x}$, $Fe_2V_{1+x}Al_{1-x}$, $Fe_{2-x}V_{1+x}Al$ at 300 K.

Nom. composition	**α (μV/K)**	**ρ (μΩ.m)**	***PF* (mW.m^{-1}.K^{-2})**
$Fe_2V_{0.93}Al_{1.07}$	38.4	1.1	1.33
$Fe_2V_{0.95}Al_{1.05}$	49.8	1.21	2.05
$Fe_2V_{0.97}Al_{1.03}$	60.77	1.33	2.78
$Fe_2V_{0.985}Al_{1.015}$	89.5	2.5	3.20
Fe_2VAl	84.7	5.8	1.24
$Fe_2V_{1.02}Al_{0.98}$	-146.6	4.76	4.52
$Fe_2V_{1.03}Al_{0.97}$	-151.6	3.94	5.84
$Fe_2V_{1.08}Al_{0.92}$	-110.1	2.18	5.57
$Fe_{1.92}V_{1.08}Al$	-101.1	15.42	0.66
$Fe_{1.95}V_{1.05}Al$		13.79	
$Fe_{1.96}V_{1.04}Al$	-4.2	12.26	0.09
$Fe_{2.04}V_{0.96}Al$	92.3	5.26	1.61
$Fe_{2.08}V_{0.92}Al$	79.0	6.33	0.98
$Fe_{1.92}VAl_{1.08}$	93.2	9.87	0.88
$Fe_{1.95}VAl_{1.05}$		13.17	
$Fe_{2.04}VAl_{0.96}$	2.9	8.06	0.001
$Fe_{2.08}VAl_{0.92}$	-108.7	7.59	1.56

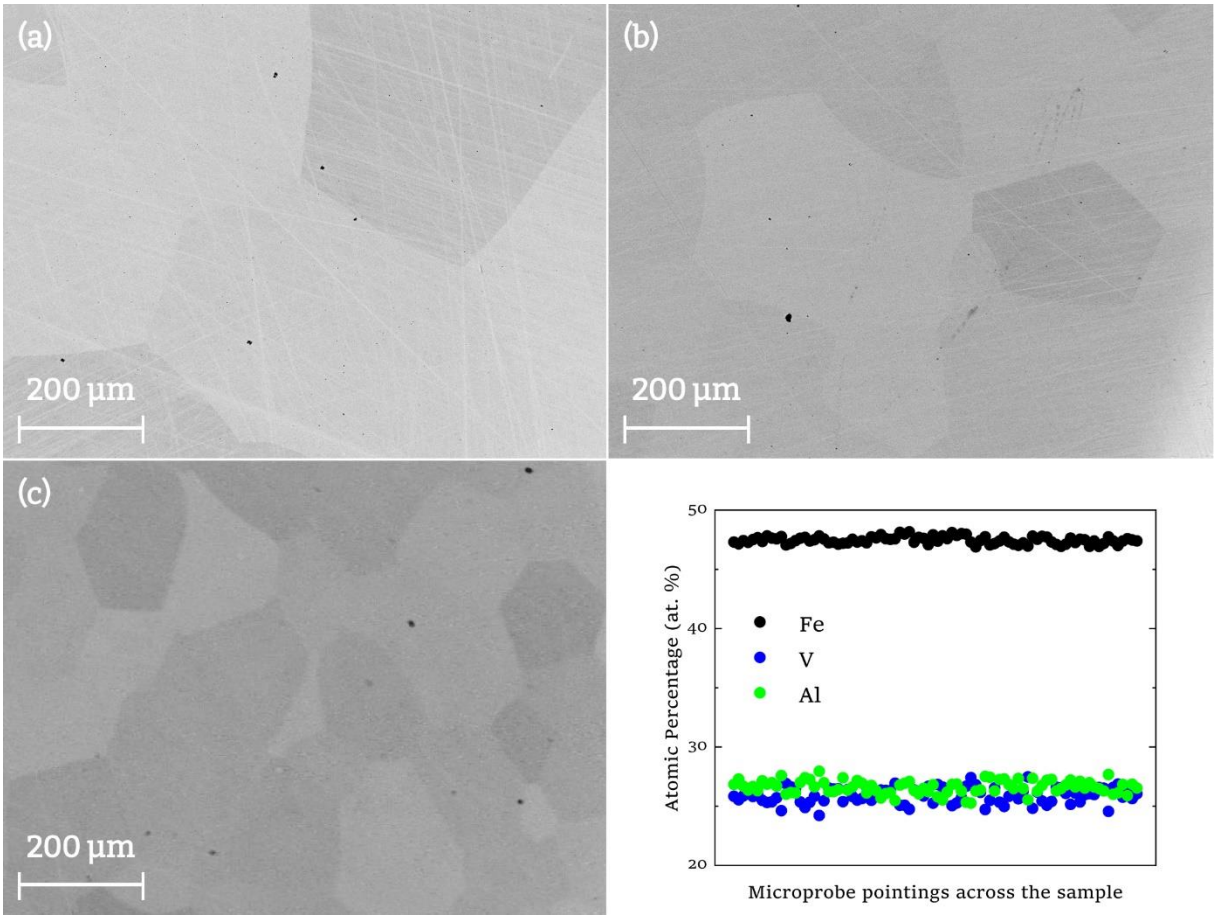

Figure 1. Back-scattered electron images of 3 samples: (a) $Fe_2V_{0.95}Al_{1.05}$, (b) $Fe_{1.96}V_{1.04}Al$, (c) $Fe_{1.92}VAl_{1.08}$ (nominal composition); (d) Fe, V, Al atomic percentage as a function of electronic microprobe (EPMA) position for $Fe_{1.92}VAl_{1.08}$.

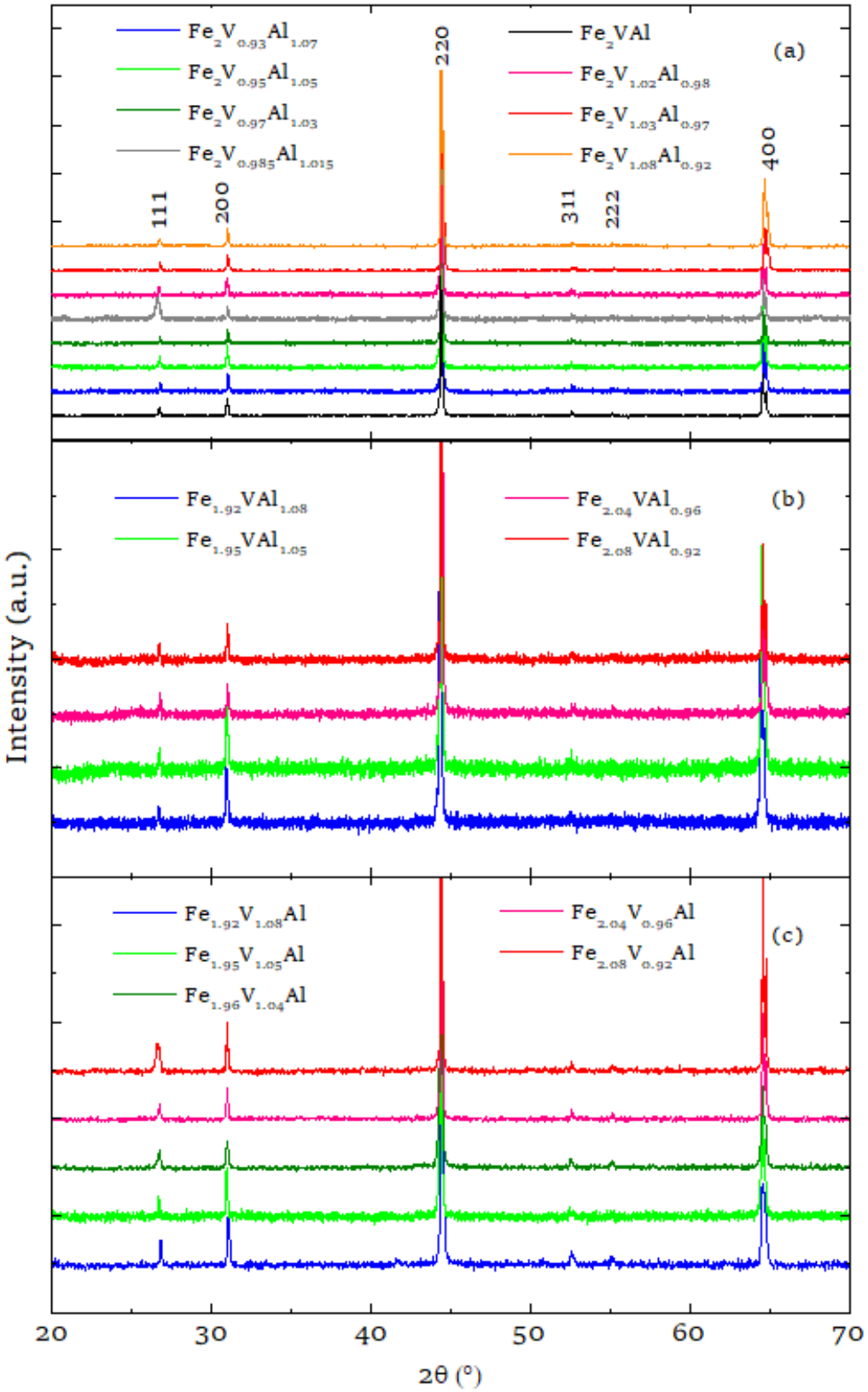

Figure 2. XRD patterns of the alloys series (a) $Fe_2V_{1+x}Al_{1-x}$; (b) $Fe_{2+x}VAl_{1-x}$; (c) $Fe_{2-x}V_{1+x}Al$.

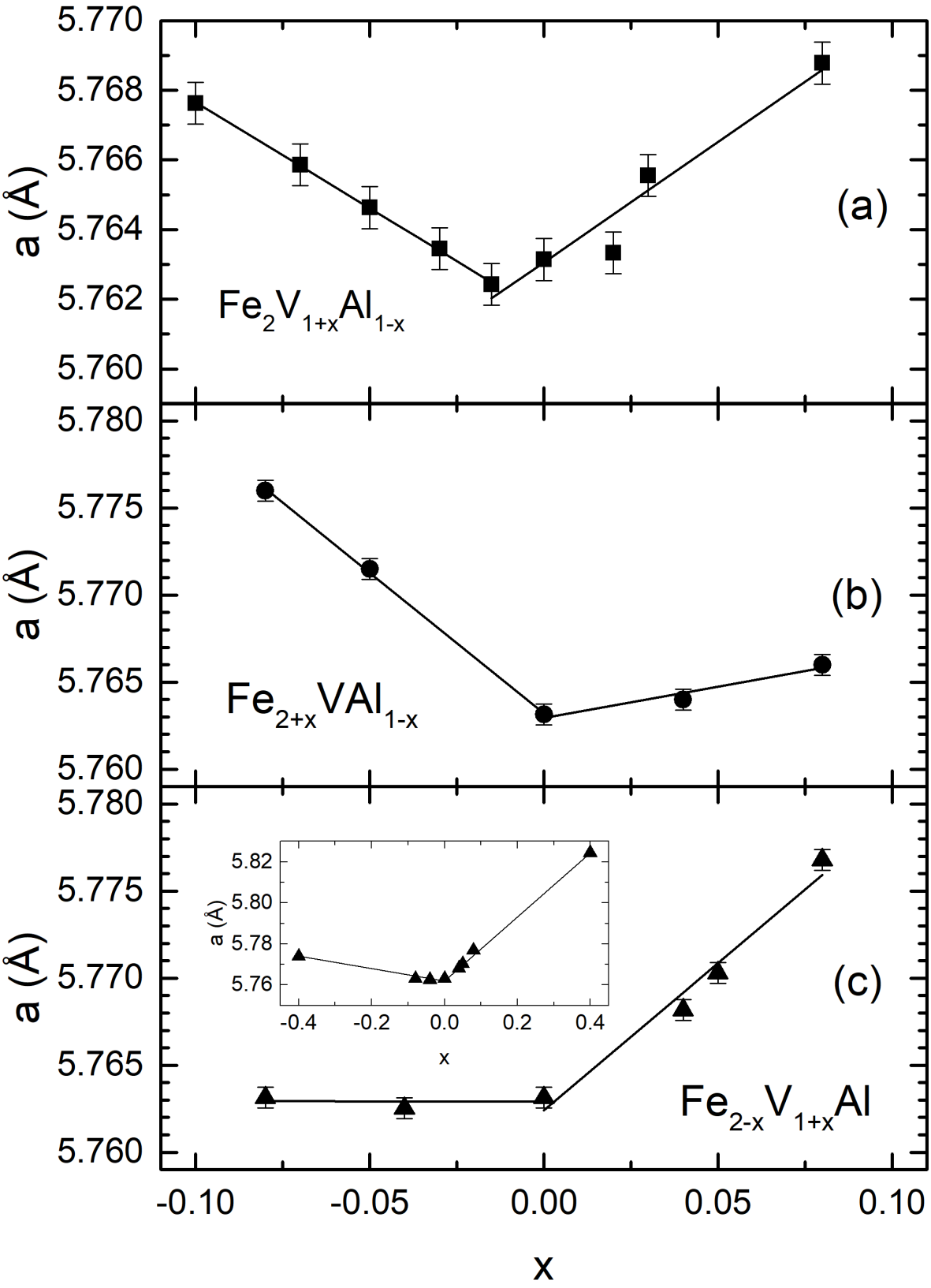

Figure 3. Evolution of lattice parameters as a function of *x* in (a) $Fe_2V_{1+x}Al_{1-x}$, (b) $Fe_{2+x}VAl_{1-x}$ and (c) $Fe_{2-x}V_{1+x}Al$ alloy series. The lines are linear fits to the data.

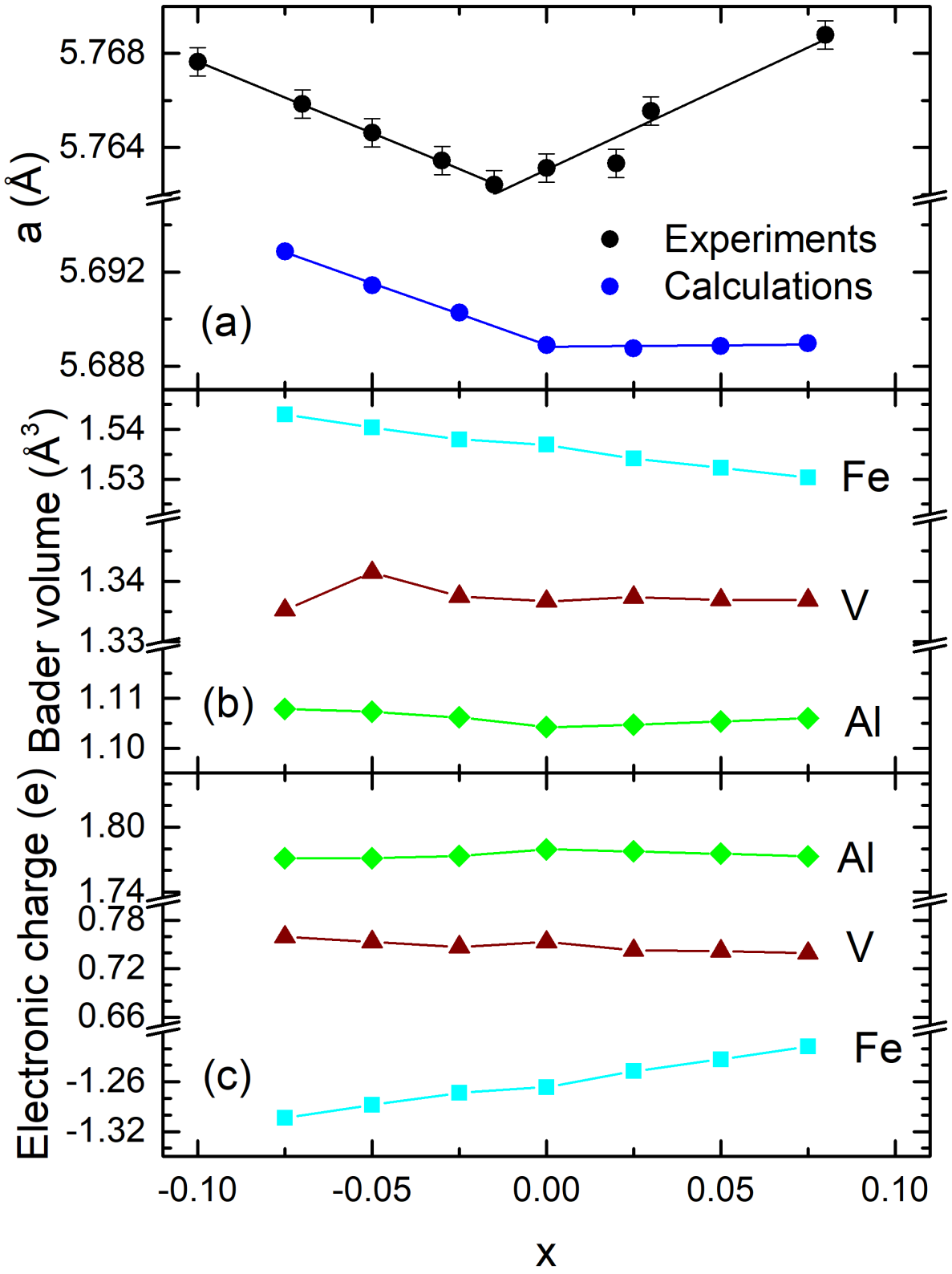

Figure 4. Evolution as a function of x in $Fe_2V_{1+x}Al_{1-x}$ of (a) the experimental and calculated lattice parameters, (b) Bader volumes of Fe, V and Al and (c) electronic charge of Fe, V and Al. For a given graph, there is no change of scale across the vertical axis.

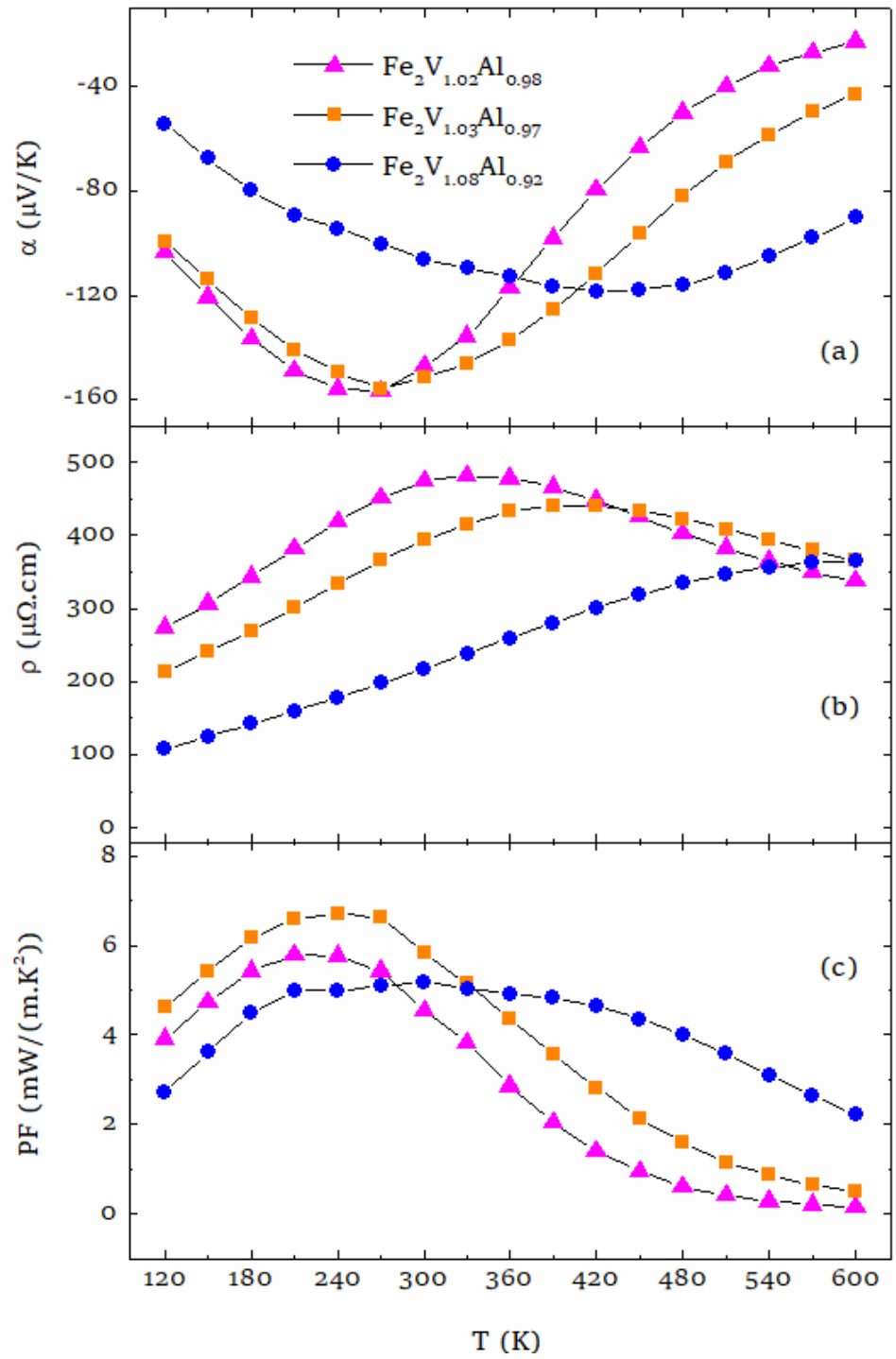

Figure 5. Seebeck coefficient (a), resistivity (b) and power factor (c) in *n*-type $Fe_2V_{1+x}Al_{1-x}$ alloys between 120 K - 600 K.

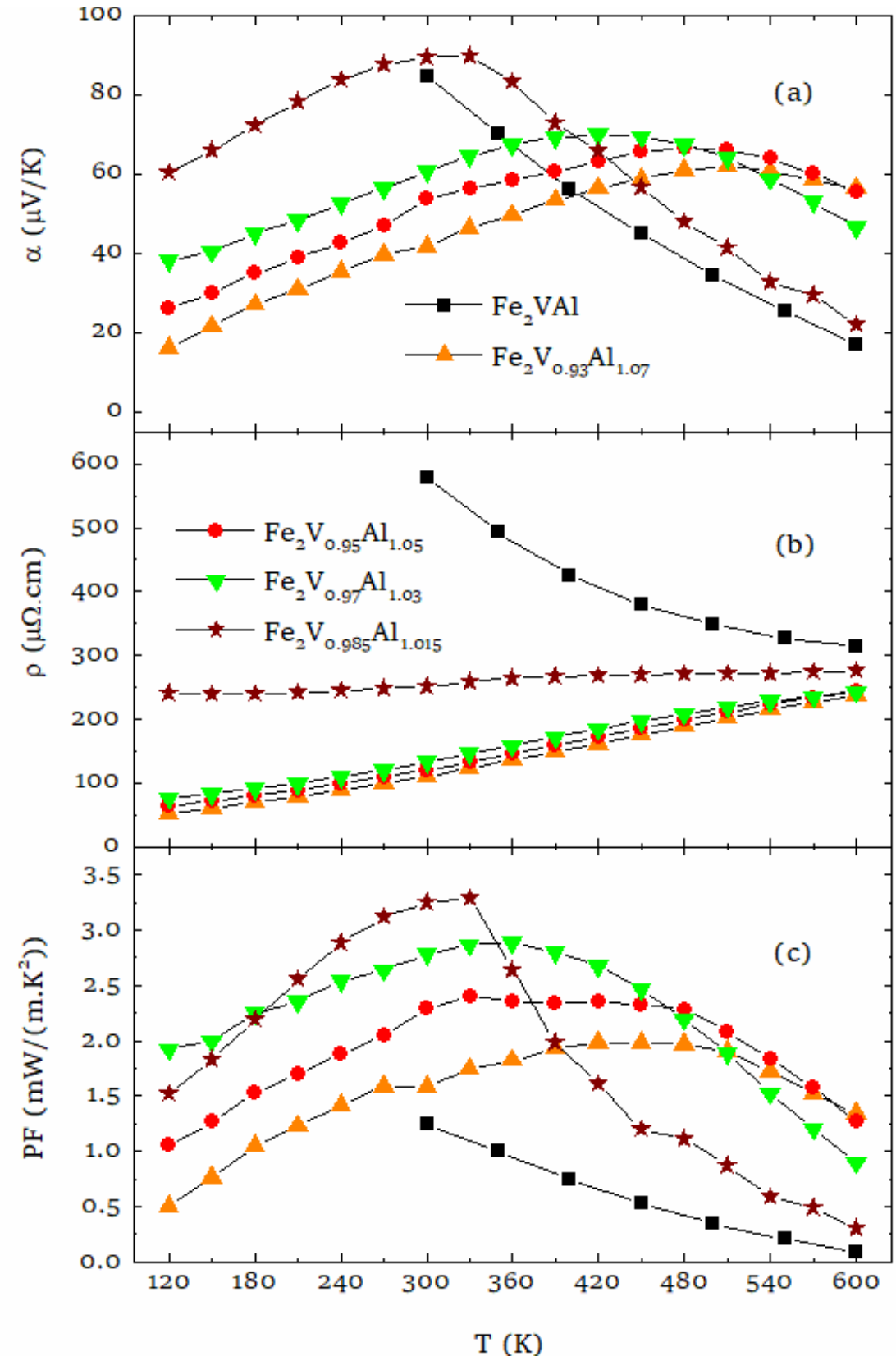

Figure 6. Seebeck coefficient (a), resistivity (b) and power factor (c) in *p*-type $Fe_2V_{1+x}Al_{1-x}$ alloys between 120 K - 600 K.

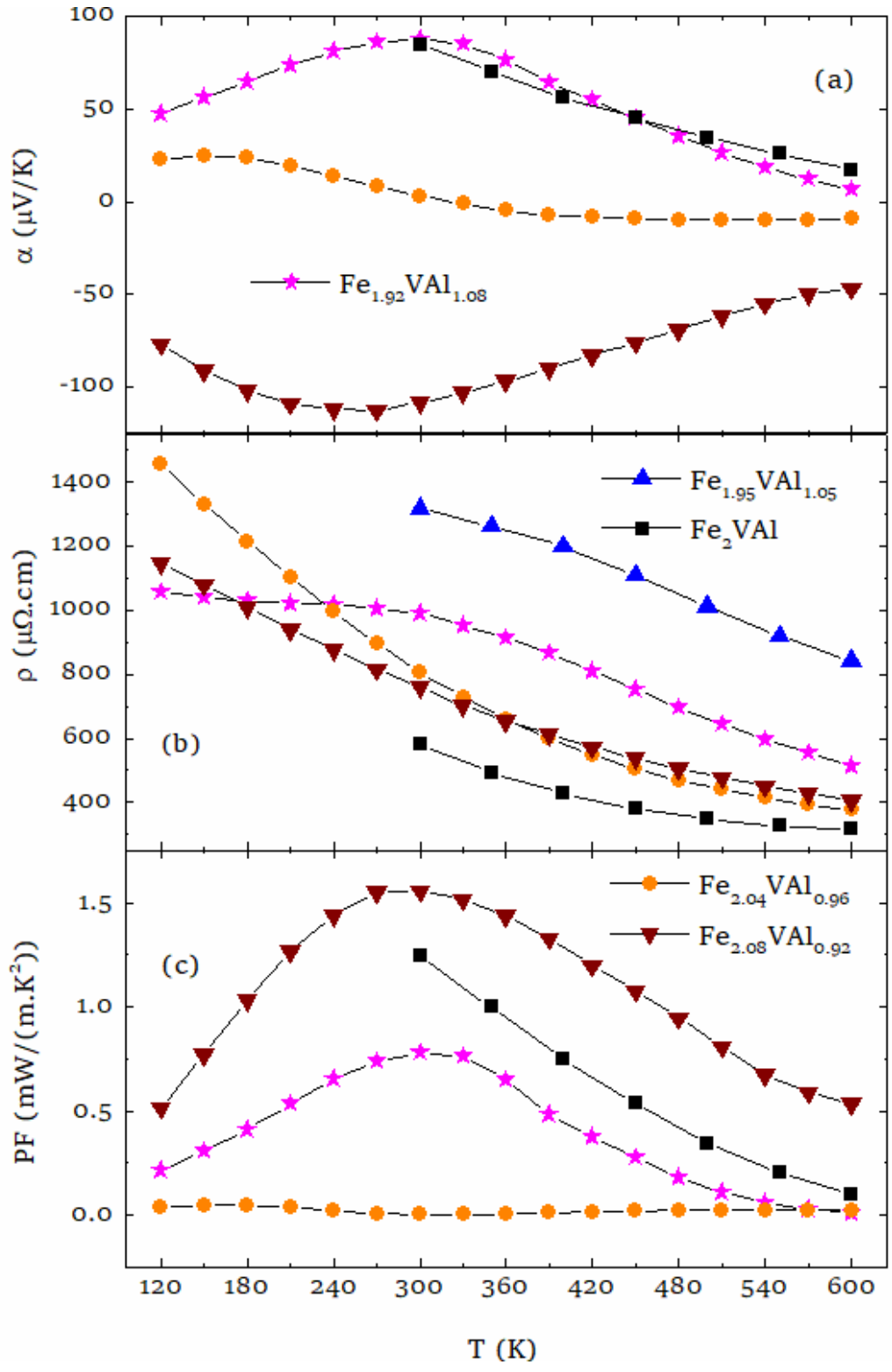

Figure 7: Seebeck coefficient (a), resistivity (b) and power factor (c) in *p*-type and *n*-type $Fe_{2+x}VAl_{1-x}$ alloys between 120 K - 600 K.

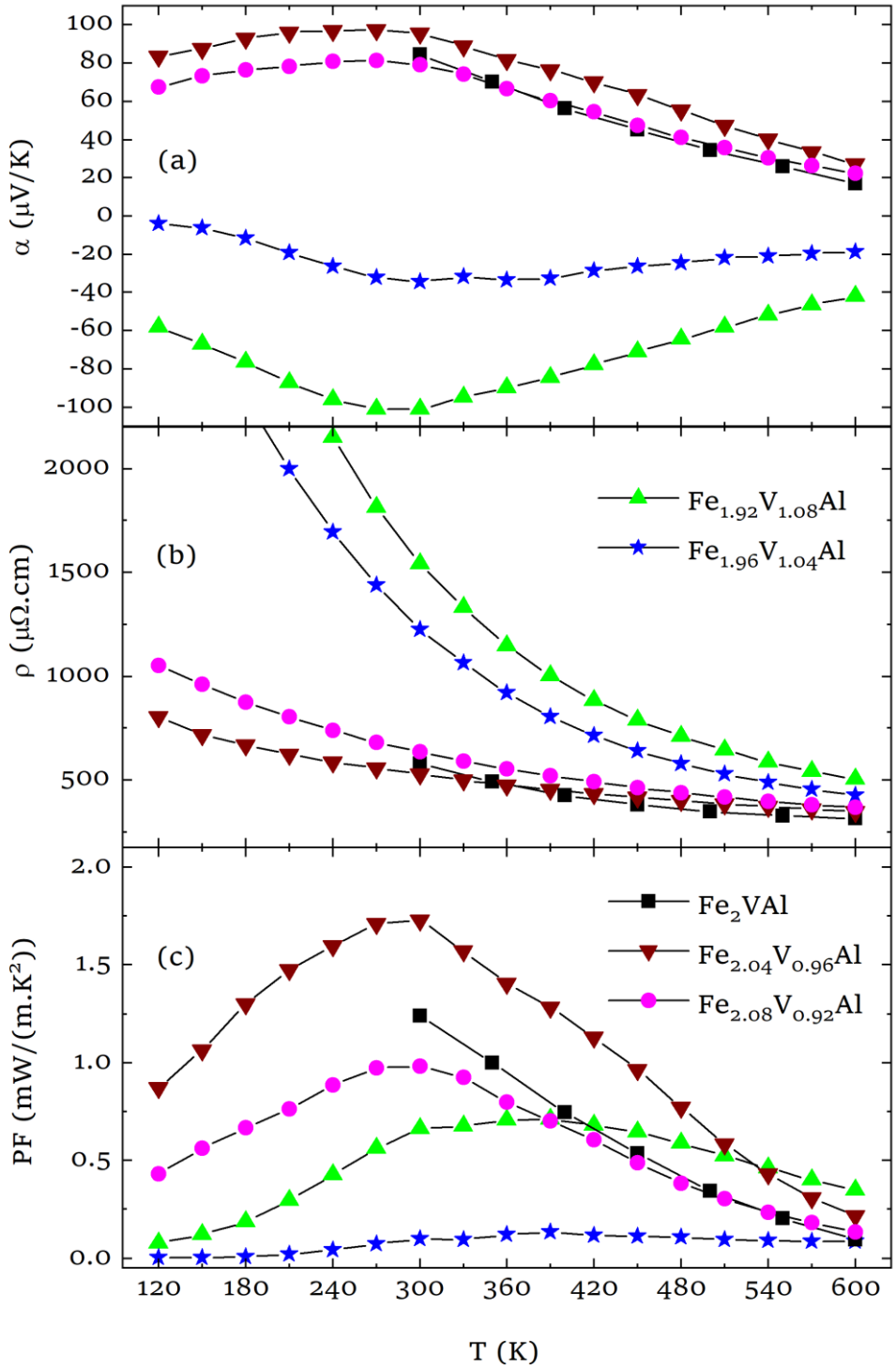

Figure 8. Seebeck coefficient (a), resistivity (b) and power factor (c) in *p*-type and *n*-type $Fe_{2-x}V_{1+x}Al$ alloys between 120 K - 600 K.

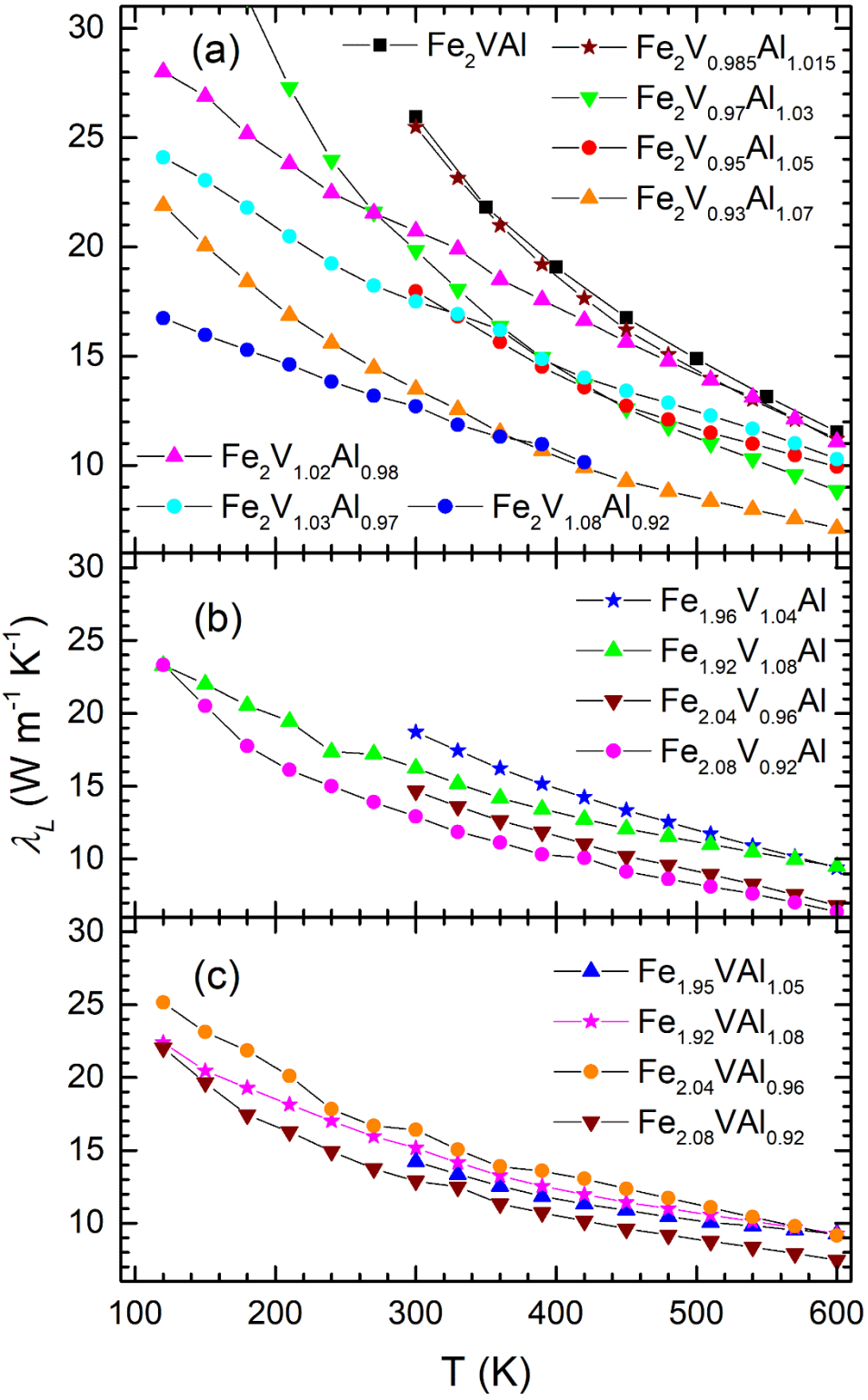

Figure 9. Lattice thermal conductivity versus temperature between 120 K - 600 K in $Fe_2V_{1+x}Al_{1-x}$ (a), $Fe_{2-x}V_{1+x}Al$ (b) and $Fe_{2+x}VAl_{1-x}$ (c) alloys.

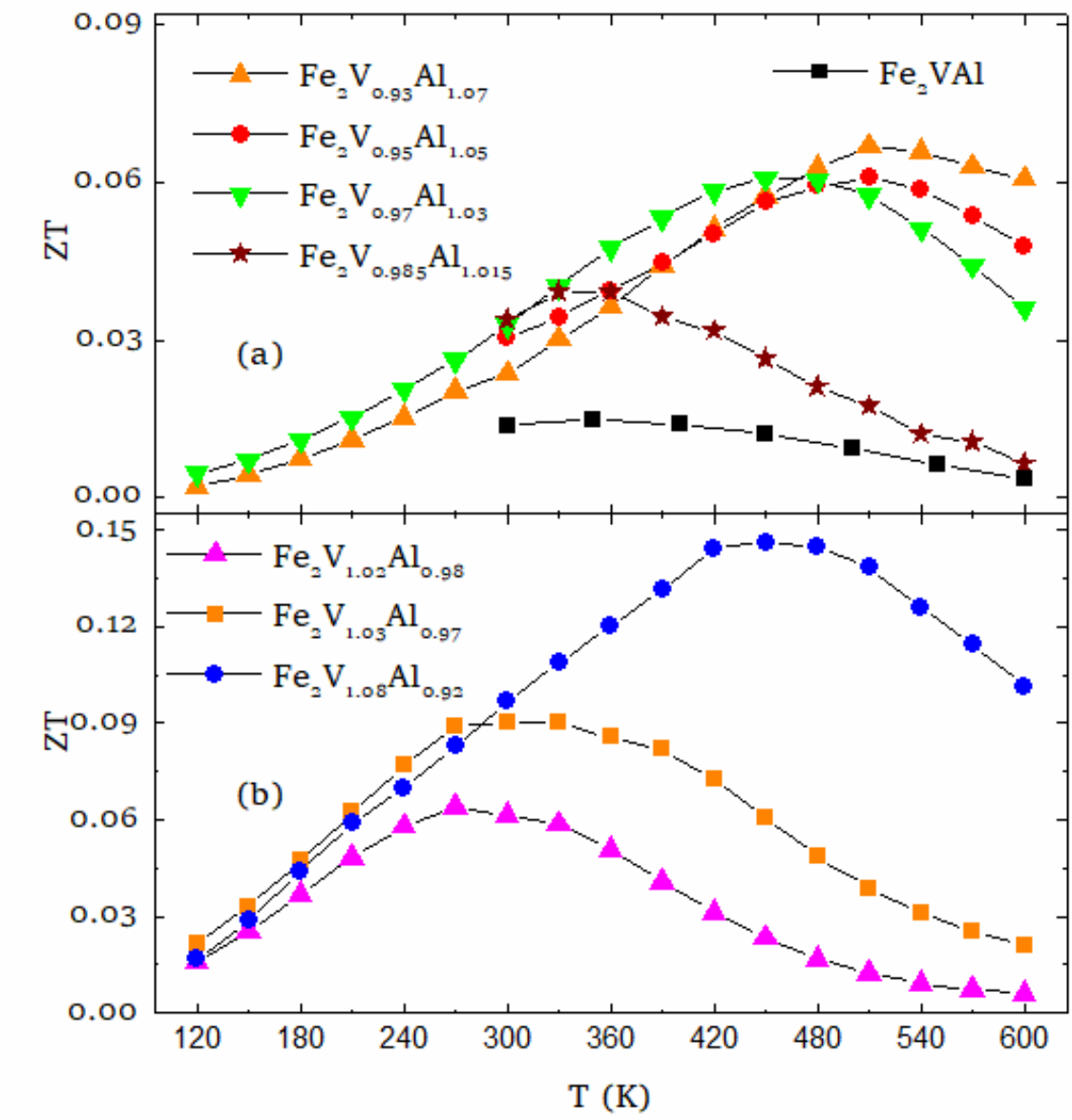

Figure 10. Dimensionless figure of merit versus temperature in $Fe_2V_{1+x}Al_{1-x}$ (a) *p*-type and (b) *n*-type alloys between 120 K - 600 K.

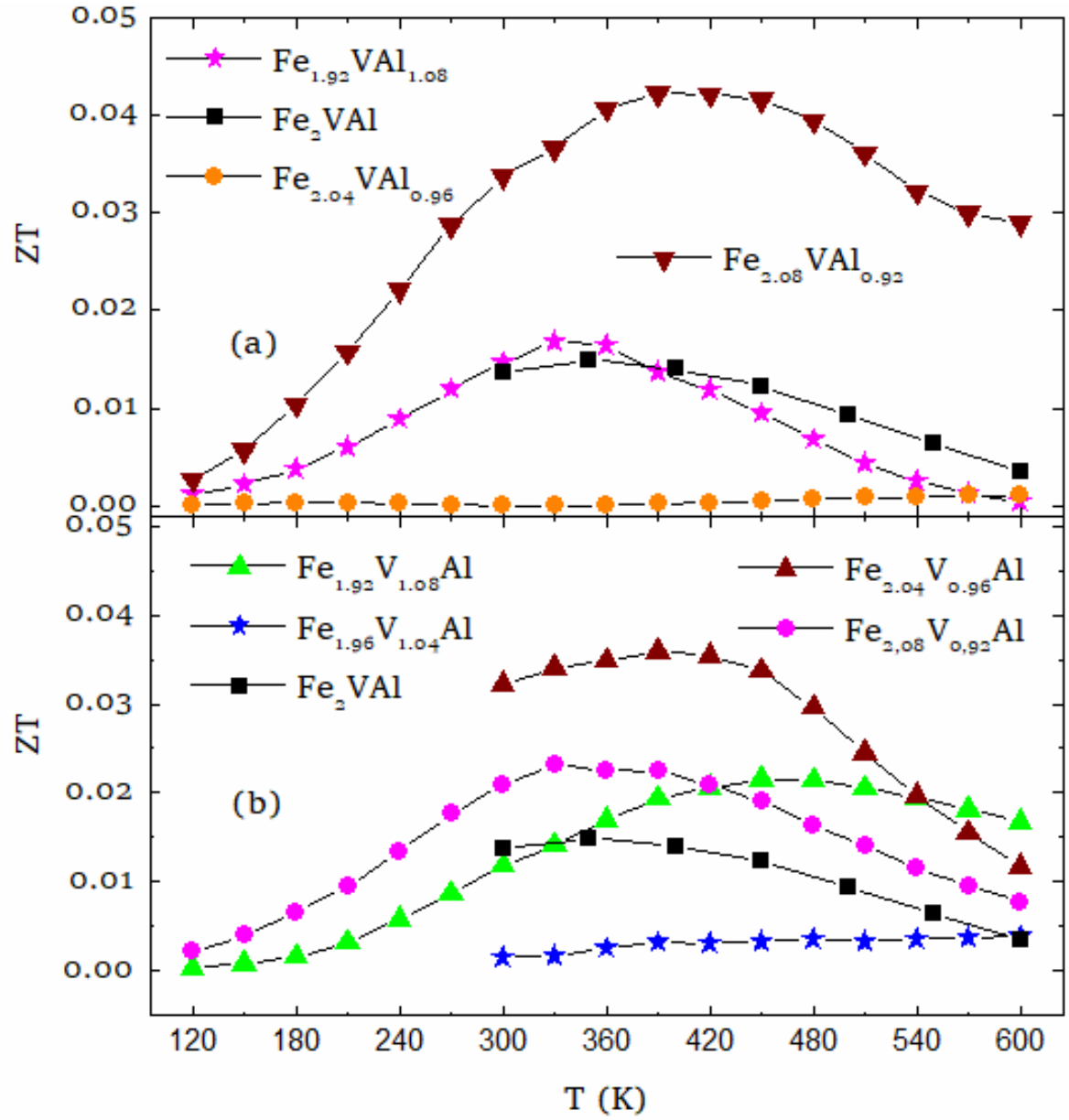

Figure 11. Dimensionless figure of merit versus temperature in (a) $Fe_{2-x}VAl_{1+x}$ and (b) $Fe_{2+x}V_{1+x}Al$ alloys between 120 K - 600 K.